Draft version September 2, 2015
Preprint typeset using LaTeX style emulateapj v. 5/2/11

arXiv:1412.8456v4 [astro-ph.CO] 1 Sep 2015

A DYNAMICALLY DRIVEN, UNIVERSAL THERMAL PROFILE OF GALAXY GROUPS AND CLUSTERS

Ido Reiss[1,2] and Uri Keshet[1]

Draft version September 2, 2015

ABSTRACT

Large scale structures such as groups and clusters of galaxies show a universal, nearly linear entropy radial profile $K(r)$. Using 16 deprojected clusters and 12 deprojected groups from the literature, we find that $K \propto r^{0.96\pm0.01}$, consistent with the mean power-law index (0.9–1.1) of previous studies. A similarly good fit is given by a $\tau \propto r^{0.72\pm0.01}$ ratio between cooling and free-fall times. Both profiles slightly flatten at small radii, as τ becomes of order unity. The entropy profile is usually attributed to self-similar shock accretion (shown to be inconsistent with the data), to non-standard heat conduction, or to turbulent heating. We argue that a dynamical mechanism is needed to sustain such a universal profile, oblivious to the temperature peak at the edge of the core and to the virial shock at the outskirts, and robust to the presence of ongoing cooling, merger, and active galactic nucleus activity. In particular, we show that such a profile can be naturally obtained in a spiral flow, which is likely to underlie most galaxy aggregates according to the ubiquitous spiral patterns and cold fronts observed. Generalizing a two-phase spiral flow model out to the virial radius surprisingly reproduces the thermal profile. A generalized Schwarzschild criterion indicates that observed spiral patterns must involve a convective layer, which may regulate the thermal profile.

Subject headings: galaxies: clusters: general — hydrodynamics — intergalactic medium — X-rays: galaxies: clusters

1. INTRODUCTION

Most groups and clusters of galaxies (galaxy aggregates; henceforth GAs) show a central dense, cool core (CC) in which the radiative cooling time of the intergalactic medium (*i.e.,* intragroup or intracluster; henceforth IGM) is shorter than the age of the GA. Some quasi-steady, smoothly distributed heat injection mechanism is needed in order to balance the observed cooling, and to sustain the only mild (factor of a few, typically) temperature drop toward the center. For reviews of such CC GAs and possible heating mechanisms, see Peterson & Fabian (2006); McNamara & Nulsen (2007); Soker (2010); Fabian (2012); Kravtsov & Borgani (2012); Cavaliere & Lapi (2013); Vikhlinin et al. (2014).

Energetically, core cooling can plausibly be suppressed, for example, by thermal conduction (Zakamska & Narayan 2003) that is modified by heat buoyancy instabilities (Quataert 2008), or by the energy output of the active galactic nucleus (AGN) in the central cD galaxy (*e.g.,* Bîrzan et al. 2004). In particular, sufficient mechanical energy is thought to be deposited in hot AGN bubbles (Churazov et al. 2002), which are found in at least 70% of the CCs (Dunn & Fabian 2006). However, it is unclear if the energy can be transferred steadily and homogeneously throughout the cooling plasma, in order to stem the local thermal instability. Moreover, a feedback mechanism is needed in order to regulate the heating and adapt to changes in the core. If the AGN output is regulated by the accreted, cooling plasma, it could furnish such a feedback loop and quench the global thermal instability as well (*e.g.,* Rafferty et al. 2008).

[1] Physics Department, Ben-Gurion University of the Negev, POB 653, Be'er-Sheva 84105, Israel
[2] Physics Department, Nuclear Research Center Negev, POB 9001, Be'er-Sheva 84190, Israel

The thermal structure of an observed GA is often characterized by the azimuthally averaged, radial profiles of electron number density n_e and temperature T. To gauge the non-adiabatic processes, in particular radiative cooling, shock heating, and heat conduction, it is useful to study the adiabat, conventionally referred to as the 'specific entropy' or just 'entropy' (henceforth), $K = n_e^{-2/3} k_{\rm B} T$, where $k_{\rm B}$ is the Boltzmann constant (*e.g.,* Voit et al. 2005; Cavagnolo et al. 2009).

Using a simplified spherical model, and in the absence of radiative cooling, AGN feedback, and star formation, Tozzi & Norman (2001) found that the radial entropy profile has a power-law behavior at large radii, $K \propto r^{\lambda_K}$, with $\lambda_K \approx 1.1$. Later, full cosmological simulations (Voit et al. 2005, henceforth V05) have shown that the radial entropy profile would be nearly constant near the center ($r \lesssim 0.1 R_{200}$), and approach a power-law profile at large radii ($r \gtrsim 0.1 R_{200}$), such that $K \simeq K_0 + \bar{K} r^{\lambda_K}$. Here, R_x is the radius enclosing a mean density x times larger than the critical density of the Universe. The power-law indices were fit as $\lambda_K = 1.21 \pm 0.01$ for the SPH code, and $\lambda_K = 1.24 \pm 0.03$ for the AMR code; henceforth we refer to this as $\lambda_K \approx 1.2$, for brevity. After scaling the entropy of a GA of mass M by the mass dependent factor $K_M \propto M^{0.26}$ (V05), $(\bar{K}/K_M)$ was found to vary among GAs by only $\lesssim 3\%$, but different codes give constants (K_0/K_M) that differ by a factor of ~ 2.

Several studies of the observed entropy profiles in GAs were previously presented, as summarized in Table 1. Various methods were used. Some works analyzed the entropy K as a function of radius r, while others studied the scaled entropy as a function of the scaled radius, $h(z)^{4/3} T^{-0.65} K = K_{\rm norm} (r/0.1 R_{200})^{\lambda_K}$ (*e.g.,* Ponman et al. 2003; Pratt & Arnaud 2005). Here, z is the redshift, $h^2(z) \equiv \Omega_m (1+z)^3 + \Omega_\Lambda$, and Ω_m, Ω_Λ are

the matter, vacuum energy fractions. Both pure radial power laws and power laws with a constant core, $K = K_0 + K_{100}\,(r/100\ \mathrm{kpc})^{\lambda_K}$, were considered. Some studies used the deprojected T, others fitted a parametric model for T, and some simply used the projected T.

In general, results that are not fully deprojected should be treated with caution, as the projection effects (*e.g.,* Panagoulia et al. 2014) and the exact model fitted (*e.g.,* Pratt et al. 2006) can have a significant effect on the results. This can explain some but not all of the apparent inconsistencies in the table. The deprojected samples, when averaged, give $\lambda_K \sim (0.9\text{–}1.1)$. Panagoulia et al. (2014) found no evidence for an 'entropy floor' in the centers of GAs, and suggested that the floor found by others (*e.g.,* Cavagnolo et al. 2009) may be due to a combination of resolution and projection effects. No redshift dependence was found in the $z \in [0.1\text{–}1]$ range within $r < 0.7R_{500}$ (Pratt et al. 2010).

In the past decade, high resolution X-ray observations have revealed the presence of spiral patterns in a significant fraction of the CC clusters for which high quality data are available (*e.g.,* Clarke et al. 2004; Tanaka et al. 2006; Sanders et al. 2009; Johnson et al. 2010; Laganá et al. 2010; Randall et al. 2010; Blanton et al. 2011; Roediger et al. 2011; Nulsen et al. 2013; Venturi et al. 2013; Giacintucci et al. 2014; Ghizzardi et al. 2014; Sanders et al. 2014). These observations suggest a spiral morphology composed of spatially alternating, low entropy and high entropy plasma phases, which are approximately at a local pressure equilibrium. Recent, deep observations found hints of spiral patterns in clusters on a much larger, Mpc scale (Simionescu et al. 2012; Rossetti et al. 2013; Walker et al. 2014). Lately, deep observation of CC groups revealed similar features (Gastaldello et al. 2009b; Randall et al. 2009; Machacek et al. 2011; Canning et al. 2013; Gastaldello et al. 2013).

The boundary between the low entropy phase from below (*i.e.,* closer to the center of the GA), and the high entropy phase from above, may form a discontinuity, observed as an X-ray edge known as a cold front (CF) where projection effects are favorable. In CCs, CFs are the telltale signs of an underlying spiral structure. Indeed, such CFs are often quasi-spiral, piecewise spiral, or nearly concentric, suggesting an underlying three-dimensional (3D) spiral pattern seen in various projections. Multiple, quasi-concentric CFs are often found on alternating sides of the center of the GA, with an increasing distance and size, consistent with a spiral discontinuity manifold observed edge on. Examples include the clusters A2142, RXJ1720.1+2638, A2204, and A496 (Markevitch & Vikhlinin 2007, and references therein), and the group NGC5098 (Randall et al. 2009).

As a local phenomenon, CFs are easier to detect and quantify than spiral patterns. Hence, CFs provide the main evidence for the prevalence of spiral structures in GAs. CFs were found in more than half of the otherwise relaxed CCs (Markevitch et al. 2003), and nearly in all of the well-observed, low redshift cores. For example, at least one CF was found in each of the 10 CCs in the sample of Ghizzardi et al. (2010).

CFs are particularly useful for studying spiral patterns because they constrain the underlying dynamics. Indeed, such CFs typically show deviations from hydrostatic equilibrium (*e.g.,* Mazzotta et al. 2001) that reflect fast flows and shear below the CF (Keshet et al. 2010). The pressure jumps resulting from shear magnetization, predicted in CC CFs both analytically (Keshet et al. 2010) and numerically (ZuHone et al. 2011), were recently measured at the $\sim 10\%$ level (Reiss & Keshet 2014). The low entropy component below the CF is colder and denser (both by a similar factor q of up to a few) and higher in metallicity than the plasma above it (*e.g.,* Markevitch & Vikhlinin 2007; Ghizzardi et al. 2014).

The spiral pattern of CFs and the fast flow below them, when combined, indicate the presence of a spiral flow. Note that by 'spiral flow' we refer to a plasma distribution giving rise to spiral features; Lagrangian fluid elements do not necessarily follow spiral trajectories (Ascasibar & Markevitch 2006). The ubiquity of spiral patterns and CFs suggests that such spiral flows constitute an inherent part of the GA itself. Indeed, a simple spiral flow model reproduces the main thermal features of CCs, such as the density cusp, while avoiding the local thermal instability by advecting heat across and beyond the core. The model is also consistent with the nearly logarithmic spiral pattern, the properties of the projected CFs, and the fast flow along them (Keshet 2012, henceforth K12). However, the recent evidence for extended, Mpc scale spiral patterns suggests that spiral flows are, in fact, a GA-wide phenomenon.

We study the two universal properties of GAs discussed above in conjunction, namely a universal power-law entropy, or entropy-like, profile (henceforth: universal profile) and an underlying, extended spiral flow, reaching beyond the core. After evaluating the universal profile and arguing that it is likely to arise from a dynamical mechanism, we point out that a GA-wide spiral flow can naturally explain it, thus linking the two phenomena.

The paper is organized as follows. In Section 2 we analyze the entropy profiles of deprojected GAs found in the literature. We also study a different, but nearly indistinguishable measure of the thermal profile, namely the ratio between the cooling and free-fall times. In Section 3 we argue for a dynamical origin of the universal profile. We show how it naturally arises in a spiral flow, using two different arguments, in Section 4. In Section 5 we demonstrate this using a third, more rigorous argument. Here we generalize the two-phase CC spiral flow to span the entire GA, surprisingly reproducing the universal profile. Our results are summarized and discussed in Section 6.

We adopt the ΛCDM cosmological model with a Hubble constant $H_0 = 70\ \mathrm{km\ s^{-1}\ Mpc^{-1}}$. Assuming a 76% hydrogen mass fraction gives a mean particle mass $\mu = 0.59m_p$ and a particle number density $n = \zeta n_e$, where m_p is the proton mass and $\zeta \simeq 2.1$. Confidence intervals are 68% for one parameter. All fit uncertainties were estimated from the dispersion of the data points around the best fit, because propagating the measurement uncertainties of each data point makes a small (by a factor of a few) contribution to the total uncertainty.

2. A UNIVERSAL THERMAL PROFILE

2.1. *Specific Entropy Profile*

Table 1
Studies of the entropy profile

Reference (1)	Sample Size (2)	M_{500} Range (3)	Temperature (4)	K_0 (5)	K_{100} (6)	$K_{\rm norm}$ (7)	$r[kpc]$ (8)	r/R_{200} (9)	λ_K (10)
P05	5	2–8	deprojected	–	–	~ 470	–	0.01–0.8	0.94 ± 0.14
P05b	13	0.6–8.7	deprojected	–	–	504 ± 140	–	0.01–0.8	0.95 ± 0.02
M05	8	0.2–1.5	modeled	–	–	≈ 420	–	0.01–1	$0.92^{+0.04}_{-0.05}$
P06	10	0.2–1.5	modeled	–	–	≈ 400	–	0.01–0.8	1.08 ± 0.04
D06	9	1.5–10	deprojected	7.3 ± 4.6	100–210	–	1–300	–	1.2 ± 0.2
			deprojected	–	100–210	–	1–300	–	1.0 ± 0.2
S09	9	0.6–12	deprojected	–	–	349 ± 22	–	0.002–0.4	$1.05^{+0.07}_{-0.15}$
J09	12	0.3–1.3	projected	–	–	≈ 330	–	0.007–1	0.71 ± 0.02
C09	107	0.2–23	projected	16.1 ± 5.7	100–200	–	1–1000	–	1.2 ± 0.38
P10	10	1.7–13	modeled	25 ± 25	120 ± 55	–	20–1000	–	0.8–1.2
P14	66	–	deprojected	–	~ 240	–	0.2–100	–	≈ 0.9
	13		deprojected	–	~ 90	–	0.2–20	–	≈ 0.64
This work	29	0.05–9	deprojected	–	187 ± 6	–	10–2000	–	0.96 ± 0.01

Note. — **Columns:** (1) Reference abbreviations: P05—Pratt & Arnaud (2005), P05b—Piffaretti et al. (2005), M05—Mahdavi et al. (2005), P06—Pratt et al. (2006), D06—Donahue et al. (2006), S09—Sanderson et al. (2009), J09—Johnson et al. (2009), C09—Cavagnolo et al. (2009), P10—Pratt et al. (2010), P14—Panagoulia et al. (2014); (2) number of GAs in the sample; (3) mass range of the sample, within R_{500} in $10^{14} M_\odot$ units; (4) method of temperature extraction (see the text); (5) the core value K_0 [keV cm^{-2}]; (6) the constant K_{100} [keV cm^{-2}], for non-scaled fits; (7) the constant $K_{\rm norm}$ [keV cm^{-2}], for scaled fits; (8) radial range in kpc for non-scaled fits; (9) radial range in R_{200} for scaled fits; (10) entropy power-law index $\lambda_K = d \log K / d \log r$.

We examine the azimuthally averaged, deprojected radial thermal profiles of GAs from the literature. The GAs analyzed are summarized in Table 2. The sample is composed of GAs with a relatively low redshift, $z < 0.25$. They span a wide range of masses, $M_{500} = [0.05 - 9] \times 10^{14} M_\odot$, where M_{500} is the mass enclosed inside R_{500}.

We compute K for each radial data bin in each GA. Following Panagoulia et al. (2014), we remove the innermost data point in each GA in order to reduce resolution effects. The number density n_e is derived from the deprojected X-ray surface brightness, $F_{\rm X}$.

The temperature T is derived using two different methods: (i) by deprojecting the same X-ray data used for n_e; or (ii) by combining n_e derived from ROSAT $F_{\rm X}$ maps, with the electron thermal pressure, $P \equiv k_{\rm B} T \zeta n_e$, derived from the Sunyaev–Zel'dovich (SZ) effect measured by *Planck* (Eckert et al. 2012, 2013b; Planck Collaboration et al. 2013). These two methods agree well where they overlap (A1795, A2029, A3112, A2052, and A2204), showing that the systematic errors in the temperatures derived are small.

In Figure 1 the entropy K is plotted as a function of radius for all the GAs of our sample. For clarity, individual measurement uncertainties are not shown. The results are well-fit ($1 - R^2 \simeq 0.072$) in the $r \simeq [0.01–2]$ Mpc range by a pure power law,

$$K = K_{100} \, (r/100 \text{ kpc})^{\lambda_K} \ , \qquad (1)$$

with

$$\lambda_K = 0.96 \pm 0.01; \quad \text{and} \quad K_{100} = 187 \pm 6 \text{ keV cm}^2 \, , \qquad (2)$$

and with a fractional dispersion $\sigma(\log_{10} K_{100}) \simeq 0.4$. Deviations from this power-law are seen for $r \lesssim 10$ kpc, where $K(r)$ slightly flattens.

Using a smaller radial extent, $[0.3–1.5] R_{500}$ (similar to V05), gives $\lambda_K = 1.00 \pm 0.05$. Fitting the scaled entropy to the scaled radius gives $\lambda_K = 0.96 \pm 0.01$ for $r > 10$ kpc, but the fit is not as good ($1 - R^2 \simeq 0.12$) as it is for the non-scaled fit.

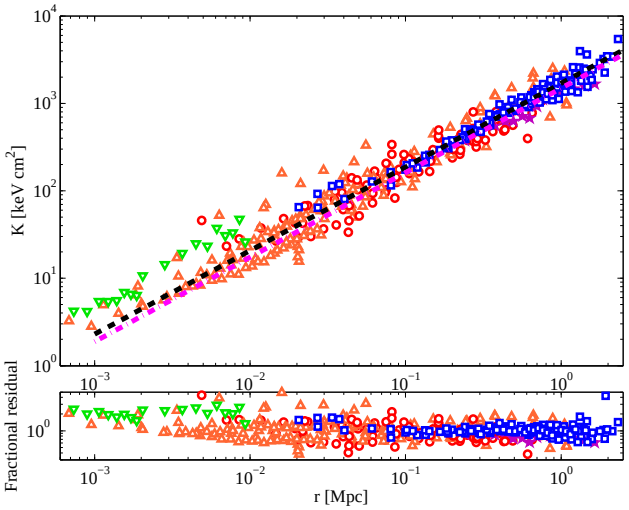

Figure 1. Top: specific entropy K as a function of radius, for all radial bins of all objects in the sample (Table 2). The temperature used to compute K was derived either from the deprojection of X-ray spectra (red circles: *XMM-Newton*; orange triangles: *Chandra*; purple pentagram: *Suzaku*) or from the SZ pressure (blue squares). Also shown are data for M49 (green down triangles), the $r > 10$ kpc power-law fit for the entire data (dashed black; Equation (2)), and the weighted mean over individual GA fits (dotted-dashed magenta; Equation (3)). Bottom: the fractional residuals from the power-law fit to all the data; Equation (2).

Each GA can be separately fit with a power-law profile. The (uncertainty weighted) mean over all GAs then gives

$$\lambda_K^{sep} = 0.97 \pm 0.01; \quad \text{and} \quad K_{100}^{sep} = 153 \pm 2 \text{ keV cm}^2 \, , \qquad (3)$$

but there is a considerable scatter, $\sigma(\lambda_K) = 0.20$ and $\sigma(K_{100}) = 72$ keV cm^2, among different GAs. The scatter in K_{100} is largely due to two outlier GAs; see Figure 3.

Figures 2 and 3 show λ_K and K_{100}, respectively, as a function of the GA mass, for individual GAs with sufficient data (more than 4 data points beyond 10 kpc). Neither λ_K nor K_{100} show a correlation with M_{500}. Note that a $K_{100} \propto M^{0.26}$ correlation would be expected in

Table 2
Sample details.

GA Name (1)	Deprojection Reference (2)	*Planck* SZ (3)	M_{500} (4)
2A0335	Kaastra et al. (2004)	–	1.62
A0085	–	✓	5.06
A0262	Kaastra et al. (2004)	–	0.68
	Sanders et al. (2010)		
A0399	Kaastra et al. (2004)	–	7.44
A0478	–	✓	8.42
A0496	Kaastra et al. (2004)	–	2.04
A1795	ibid	✓	7.21
A1835	ibid	–	6.33
A1837	ibid	–	1.46
A2029	Lewis et al. (2003)	✓	8.67
A2052	Kaastra et al. (2004)	✓	1.42
A2204	Sanders et al. (2009)[a]	✓	6.44
A3112	Bulbul et al. (2012)	✓	3.83
A3581	Sanders et al. (2010)	–	0.70
A4059	Kaastra et al. (2004)	–	2.93
AWM4	O'Sullivan et al. (2010)	–	1.04
HCG62	Gitti et al. (2010)	–	0.29
	Sanders et al. (2010)		
M49	Kraft et al. (2011)	–	0.94[b]
MKW9	Kaastra et al. (2004)	–	0.88
NGC0533	ibid	–	0.32
NGC0741	Jetha et al. (2008)	–	0.70
NGC4261	O'Sullivan et al. (2011)	–	0.77
NGC5813	Randall et al. (2011)	–	0.18
NGC4325	Russell et al. (2007)	–	0.23
NGC4636	Werner et al. (2009)	–	0.11
NGC6482	Khosroshahi et al. (2004)	–	0.05
Perseus	Churazov et al. (2003)	–	4.97
	Urban et al. (2014)		
RXJ1159	Humphrey et al. (2012)	–	0.59
Virgo	Kaastra et al. (2004)	–	0.94

Note. — **Columns:** (1) GA name; (2) deprojected temperature data reference; (3) existence of SZ data (Eckert et al. 2012, 2013b; Planck Collaboration et al. 2013); (4) cluster mass $[10^{14} M_{\odot}]$ (Reiprich & Böhringer 2002; Osmond & Ponman 2004; Piffaretti et al. 2005; Pratt & Arnaud 2005; Finoguenov et al. 2006; Gastaldello et al. 2009a; Eckmiller et al. 2011; Urban et al. 2011; Humphrey et al. 2012).

[a] Showing the four sectors separately.

[b] Mass of the host cluster, Virgo.

the non-radiative, accretion-only models (V05) discussed above.

As these results show, the uncertainty in the power-law index λ_K, if the latter is assumed to be a universal constant, is very small and dominated by the inherent dispersion. The power-law fits (Equations (2) and (3)) are shown in Figures 1–3 as dashed and dotted-dashed lines.

It is interesting to examine if the above universal thermal profile also applies to giant elliptical galaxies that harbor an AGN but do not lie at the center of a GA. Deprojected density and temperature profiles from *Chandra* are available (Kraft et al. 2011) for the giant elliptical M49, which resides in the outskirts of the Virgo cluster. The K and τ profiles around the galaxy, shown in Figures. 1 and 4, do indeed resemble the universal scaling. Note that the M49 data were not included in the fit formulae above, as they do not meet the $r > 10$ kpc selection criterion.

Recent *Suzaku* observations revealed a flattening in the observed entropy profile at large radii ($r \gtrsim 1$ Mpc; *e.g.*, Walker et al. 2012). This departure from a power-law

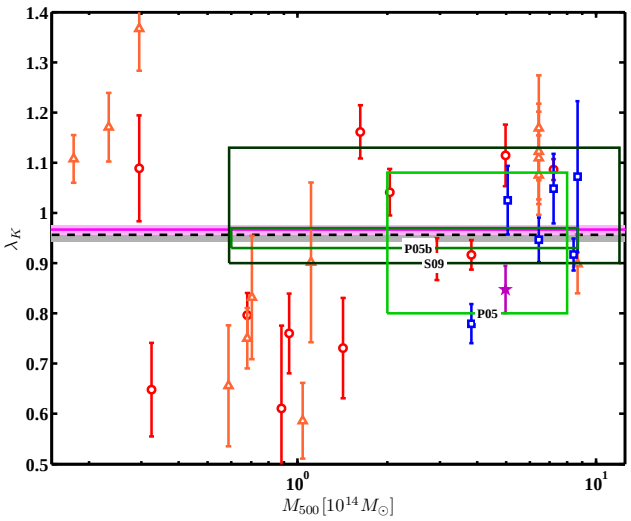

Figure 2. Specific entropy power-law index λ_K, as a function of M_{500}, in individual GAs. The symbol and line notations are the same as in Figure 1. Also shown (as labeled rectangles) are the fits of Pratt & Arnaud (2005), Piffaretti et al. (2005), and Sanderson et al. (2009).

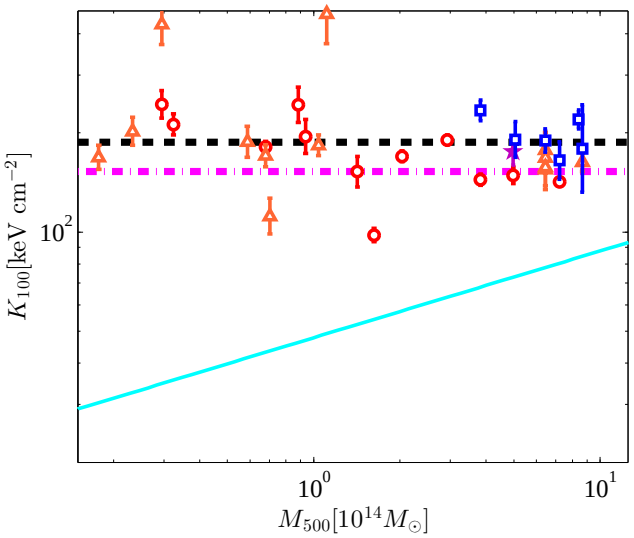

Figure 3. Specific entropy at 100 kpc, K_{100}, plotted as a function of M_{500}. The symbol and line notations are the same as in Figure 1. Also shown (solid cyan) is the entropy of the non-radiative self-similar model for $z = 0$ (V05)

behavior has been commonly attributed to gas clumping, which leads standard X-ray modeling to overestimate the gas density and thus underestimate the entropy. No significant flattening is seen in the data shown in Figure 1 (see also Appendix A), possibly because the effect is small in the relevant radial range (see, *e.g.,* Eckert et al. 2013c), or due to some bias in the *Suzaku* observations (see, *e.g.,* Morandi et al. 2015). Restricting the analysis to small radii, in the range 10 kpc $< r <$ 1 Mpc, gives $\lambda_K = 0.94 \pm 0.01$; slightly *flatter* than Equation (2).

2.2. *Cooling Time to Free-fall Time Ratio*

There are other ways to quantify the universal thermal profile of GAs. Following McCourt et al. (2012) and Sharma et al. (2012), we examine the ratio $\tau \equiv t_{\rm cool}/t_{\rm ff}$ between the cooling time $t_{\rm cool}$ and the free-fall time $t_{\rm ff}$ of

the IGM.

We define $t_{\rm cool}$ similarly to McCourt et al. (2012), as the ratio between the thermal energy density and the cooling rate of the X-ray emitting gas,

$$t_{\rm cool} \equiv \frac{U_{th}}{dE/dt} = \frac{(3/2)\zeta n_e k_{\rm B} T}{n_e^2 \Lambda(T)} \,. \quad (4)$$

Here $\Lambda(T)$ is the cooling function, which we adopt from Tozzi & Norman (2001), with a nominal 0.3 solar metallicity.

For simplicity, and to minimize the uncertainties, we define the free-fall time differently than McCourt et al. (2012), using the constant density approximation,

$$t_{\rm ff} \equiv (G\rho_{\rm tot})^{-1/2} = (f_{\rm g}/G\rho)^{1/2} \,. \quad (5)$$

Here G is Newton's constant, $\rho = \mu\zeta n_e$ is the mass density of the X-ray emitting gas, and $f_{\rm g} \equiv \rho/\rho_{\rm tot}$ is the gas mass fraction of the IGM, of order [2–15]% for $r/R_{500} > 0.01$ (Eckert et al. 2013a). Alternative definitions of $t_{\rm ff}$ differ from the above by a constant factor of order unity, which we omit; this bears no consequences for the following discussion.

With the above definitions, the ratio between the two timescales becomes

$$\tau \propto \left[\frac{T^{1/4}}{f_{\rm g}^{1/2}\Lambda(T)}\right] K^{3/4} \,. \quad (6)$$

The prefactor in the square parenthesis does not vary significantly with r. Hence, one may expect τ to scale roughly as $K^{3/4} \propto r^{3/4}$.

The gas fraction $f_{\rm g}$ is not well constrained, but is not thought to vary over more than an order of magnitude across a GA. As a first approximation, we thus assign it with a constant, $f_{\rm g} = 0.15$ value, and refine this assumption below. Indeed, τ is then well-fit by a pure power law in the range $r \simeq$ [0.01–2] Mpc,

$$\tau = (3.6 \pm 0.1)\, r_{10}^{0.72\pm0.01} \,, \quad (7)$$

where $r \equiv (r/10$ kpc), as shown in Figure 4. The dispersion of the fractional residuals to the fit is $\sigma = 0.3$. This power-law behavior slightly flattens for $r \lesssim 10$ kpc, which is the radius where $\tau \simeq 1$.

Using the high temperature approximation for the cooling function, $\Lambda(T) \simeq \Lambda_0 T^{1/2}$, where $\Lambda_0 \simeq 2.1 \times 10^{-27}$ erg s^{-1} cm^3 K$^{-1/2}$ (*e.g.,* Rybicki & Lightman 1986), Equation (7) can now be crudely written as

$$C\frac{(k_{\rm B}T)^{2/3}}{n_e^{2/3} r} \simeq \frac{\tau^{4/3}}{r} \simeq \frac{r_{10}^{0.04}}{L_\tau} \approx L_\tau^{-1} = (2\ {\rm kpc})^{-1} \,, \quad (8)$$

where $C \equiv [9Gk_{\rm B}\mu\zeta^3/(4f_{\rm g}\Lambda_0^2)]^{2/3}$ is a constant under the present (constant $f_{\rm g}$ and $\Lambda/T^{1/2}$) assumptions, and we defined $L_\tau \simeq 2$ kpc as the constant thus measured from $(\tau^{4/3}/r)$. Equation (8) resembles the entropy fit (Equations (1) and (2)), which may analogously be written in the form

$$\frac{k_{\rm B}T}{n_e^{2/3} r} = \frac{K}{r} \simeq 1.0\times10^{-30} r_{10}^{-0.04}\ {\rm erg\ cm} \simeq 10^{-30}\ {\rm erg\ cm} \,. \quad (9)$$

Equations (8) and (9) show that the observed GA thermal profiles are consistent with a universal constant value of either $(\tau^{4/3}/r) \propto T^{2/3}/(n_e^{2/3} r)$, or $(K/r) \propto T/(n_e^{2/3} r)$. These two quantities can be distinguished only by their slightly dissimilar temperature dependence, differing by a factor $T^{1/3}$. With the present data, it is difficult to determine which of the two quantities better describes GAs because the temperature range in each GA is quite narrow (usually less than an order of magnitude), the temperature differences between the GAs in our sample are not large, and the temperature uncertainties are considerable. Indeed, the fits in Equations (2) and (7) are presently of similar qualities ($1 - R^2 = 0.072$ and 0.070, respectively).

Equations (7) and (8) were derived by approximating $f_{\rm g}$ as a constant. This can be relaxed using estimates of $f_{\rm g}$ from the literature. Using the average radial dependence of $f_{\rm g}$ (Eckert et al. 2013a, median values) gives a poorer fit ($1 - R^2 = 0.094$) to the data. Using the estimated mass dependence of $f_{\rm g}$ (Gonzalez et al. 2013) renders the fit even worse ($1 - R^2 = 0.129$). In both cases, the quantity $(\tau^{4/3}/r)$ is found to be nearly constant, with a radial dependence weaker even than the mild $r_{10}^{0.04}$ of Equation (8).

Note that the dimensional constants on the right sides of Equations (8) and (9) are not naturally obtained from the constants that appear in the fluid equations (namely, the continuity, Euler, and energy equations; see section 5), without introducing a large number or some new dimensional constant, even if conduction and cooling are taken into account. For example, one may construct the length scale $L_0 \equiv \Lambda_0 G^{-1} k_B^{-1/2} \mu^{-3/2} \simeq 1$ Mpc from the constants in these equations, but this is larger by a factor of ~ 500 than L_τ. It would be natural if the cutoff on the thermal correlation itself (a few kpc; see Equation (8)) would somehow provide the necessary scale.

The simple power-law function $\tau(r)$ that we find, as shown in Equation. (7) and Figure 4, differs from the results of McCourt et al. (2012) in two ways. First, we find that τ monotonically decreases toward small radii rather than showing a minimum, probably because we use only deprojected data, adopt a more robust definition of $t_{\rm ff}$, and avoid a parametric model fit. This is consistent with the absence of an 'entropy floor' in our data, in accordance with Panagoulia et al. (2014). Second, we find a universal behavior for all the GAs examined, regardless of the presence of Hα filaments.

3. DYNAMIC ORIGIN OF THE UNIVERSAL PROFILE

The universality of the thermal profile discussed in Section 2, its extensive radial span, and its applicability over a wide mass range, place strong constraints on its origin. As we show, the static models proposed so far seem unable to reproduce the profile without fine tuning.

The entropy seeded by primordial gas crossing the virial shock (Tozzi & Norman 2001) would not naturally maintain the same power-law profile down to and beyond the core radius, where cooling plays a significant role on timescales shorter than the age of the GA. Rather, one would expect some break in the profile, unless some additional mechanism compensates for the radiative entropy loss. Whether or not such a mechanism exists, the primordial entropy should scale with the GA mass as $K_{100} \propto M_{500}^{0.26}$ (V05), but we find no such correlation (see Figure 3). Rather, the power-law index of the

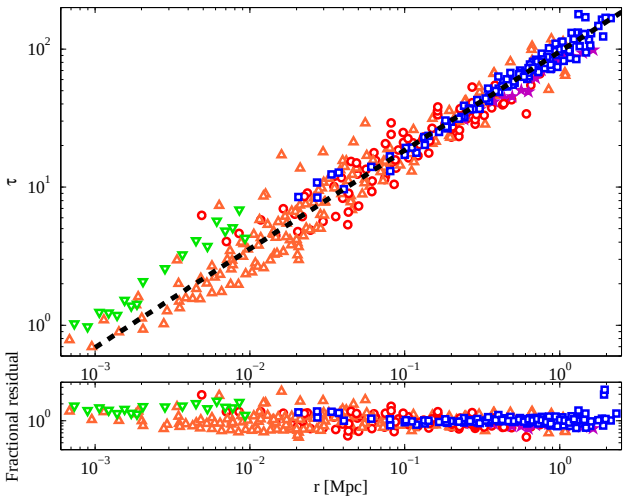

Figure 4. Top: the ratio τ between the cooling time and the free-fall time, plotted as function of radius. Bottom: the fractional residuals relative to the fit Equation (7).

$K_{100} - M_{500}$ correlation has a slightly negative best-fit, is consistent with zero ($< 2\sigma$), and is inconsistent with the predicted self similar value by $> 8\sigma$ (this applies to both SPH- and AMR-based fits of V05; henceforth). This result does not change much if the representative entropy is chosen well outside of the core (*e.g.,* $\gtrsim 5\sigma$ at 500 kpc, and $\gtrsim 4\sigma$ at 1000 kpc). Moreover, as noticed previously (*e.g.,* Pratt et al. 2010), the measured value of the entropy lies well above the prediction of the self-similar model, over the entire mass range (see Figure 3). This deviation ranges between 1σ and 20σ for individual clusters, and is $> 6.5\sigma$ for their mean. Finally, the entropy profile we find is significantly flatter (by $> 8\sigma$) than the self-similar $\lambda_K \approx 1.2$, which can be ruled out in our sample. Even by using a much smaller radial extent for the fit ($[0.3\text{–}1.5]R_{500}$, similar to V05), the self-similar prediction is still rejected by $> 4\sigma$. These arguments reject self-similar primordial accretion alone as the origin of the universal profile, and indicate a pervasive baryonic influence reaching out to the virial radius.

Another previous suggestion is that the entropy profile is governed by radial heat conduction (Zakamska & Narayan 2003; Dolag et al. 2004). This mechanism is unlikely to operate in exactly the same fashion on both sides of the temperature peak, where the radial direction of the heat flow is reversed, so again the thermal profile would naturally be broken. Moreover, Sanderson et al. (2009) showed that in order for conduction to thus explain the GA thermal profile, the heat conductivity should have a fine-tuned, unnatural functional form.

More generally, the IGM is a dynamical environment, undergoing merger activity (*e.g.,* Vikhlinin et al. 2014), susceptible to the significant energy output of the AGN (*e.g.,* Bîrzan et al. 2004), and harboring ongoing shocks (*e.g.,* Markevitch & Vikhlinin 2007), fast bulk flows (Keshet et al. 2010), and turbulence (*e.g.,* Zhuravleva et al. 2014). Static models are unlikely to robustly explain the universal profile in such surroundings.

In contrast, a dynamical mechanism, involving gas motions, could have the inertia to resist the turmoil of the IGM and stabilize the universal profile. Such a mechanism would have to operate throughout the GA, out to the virial radius, in order to modify the (mass-correlated) entropy injected by the virial shock, and to maintain the universal profile. It would also need to be insensitive to the sign of the radial temperature gradient in order to produce the same profile both inside and outside the core.

If the universal quantity turns out to be $(\tau^{4/3}/r)$, rather than (K/r), this would provide a direct indication that the process is dynamic, and is, at least on small scales, driven by gravity. The length scale $L_\tau \simeq 2$ kpc emerging from this quantity when applied to GAs (Equation (8)) would suggest a non-local effect, such as an extended bulk flow emanating from this radius.

4. SPIRAL FLOW ORIGIN OF THE UNIVERSAL PROFILE

As demonstrated by K12, spiral flows can explain the thermal structure of cores. It is natural to ask, in light of the spiral features found to extend out nearly to the virial radius, if a spiral flow reaching beyond the core can give rise to the universal profile. This is crudely examined here, and examined in more detail in the specific context of a two-phase spiral flow model in Section 5.

Consider a two-dimensional spiral flow. The more complicated, 3D case can be approximated under some assumptions as a superposition of spiral flow planes (see K12 and Section 5 below). The spiral flow necessarily involves azimuthal density and temperature gradients, as evidenced by the jumps in n_e and T across the spiral CFs. As we show, the universal profile can be recovered by making simple, although ad hoc, assumptions regarding these gradients.

First note that in order to sustain a spiral flow, mild azimuthal pressure gradients are also necessary (K12). These can be seen, for example, in Figure 5, which shows the fractional deviation of the pseudo-pressure $\tilde{P} = F_{\rm X}^{1/2}T$ from its azimuthal average, in Perseus (Churazov et al. 2003). In spite of the projection and noise, a spiral structure is clearly seen. It is highlighted by the overplotted spiral CF pattern, derived (K12) based on thresholding the $F_{\rm X}$ gradients. Indications for azimuthal pressure gradients are also seen in deprojected pressure profiles of CC GAs (Sanders et al. 2009; Urban et al. 2014).

4.1. *Scaling of the azimuthal gradients*

Next, consider the normalized azimuthal derivative $\partial \log A/\partial\phi$ of some thermal quantity $A \in \{T, P, K\}$, and in particular its radial dependence. In general, such derivatives tend to decrease with increasing radius, as the spiral sections of the flow become broader. The precise scaling would depend on the spiral pattern and on the nature of the flow. For simplicity, we assume that there exists some part of the flow in which

$$\partial_\phi \log A \propto 1/r\,. \tag{10}$$

To see how such a scaling could locally emerge, parameterize the geometric pattern of a 2D spiral by $\lambda_\gamma \equiv d\log|\gamma|/d\log(r)$, where $\gamma \equiv \tan(\alpha)$, and α is the angle between the streamline and the azimuth (K12, correcting a typo in the definition of γ therein). Thus, $\lambda_\gamma = 0$ corresponds to a logarithmic spiral, while $\lambda_\gamma = -1$ gives an Archimedean spiral. Observations, simulations, and the core spiral model suggest a nearly logarithmic spiral, with a slight Archimedean tendency,

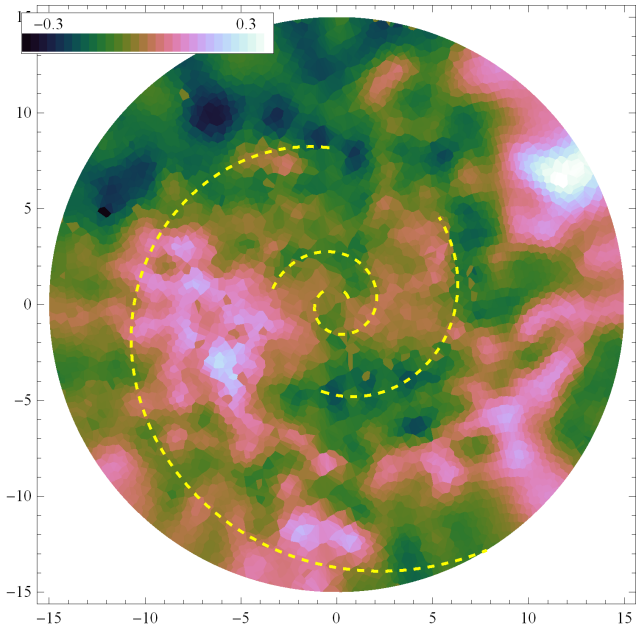

Figure 5. Fractional deviation of the pseudo-pressure $\tilde{P} = F_{\rm X}^{1/2}T$ from its azimuthal average in a 30' by 30' region around the center of Perseus (adopted from the Churazov et al. (2003) analysis of *XMM-Newton* data, courtesy E. Churazov; color scale from Green (2011)). The best-fit spiral of K12 is shown (dashed yellow) based on a gradient filter applied to $F_{\rm X}$.

$-1 < \lambda_\gamma < 0$ (K12). If the spiral structure is separable, $A = A_r(r)A_\phi(\phi - \phi_0(r))$, then $\partial \log A/\partial\phi \sim 1/\log(r)$ in a simple logarithmic spiral, and $\partial \log A/\partial\phi \sim 1/r$ in a simple Archimedean spiral.

However, neither of these spiral structures, nor any other uniform ϕ derivative, can apply globally (*i.e.*, for $0 < \phi < 2\pi$) because the CFs observed indicate that a convective layer must be embedded in the spiral structure. To see this, note that a spiral CF implies both radial and azimuthal entropy gradients. A generalized Schwarzschild criterion for convective stability then shows that a convective region must be present at any radius, as shown in Appendix B. An alternative origin for Equation. (10) would be a quasi 3D flow near the convective layer, with an effectively 2D gradient.

As the spiral structure cannot be monotonic, a simple analytic description of the entire flow is not feasible. Some regions of the spiral should, however, show a radially declining $\partial \log A/\partial\phi$ derivative. For simplicity, in the remainder of this section we assume that there exists some not necessarily large region of the flow in which T or P follow Equation (10), such that $\partial_\phi \log T \sim L/(2\pi r)$ or $\partial_\phi \log P \sim L/(2\pi r)$. Here L is some constant length scale, discussed below.

4.2. *Cooling balanced locally either by azimuthal heat conduction or radial heat advection*

Under the above assumption, consider a radiatively cooling part of the flow. The spiral structure brings hot and cold plasma phases near each other, so azimuthal heat conduction can balance the cooling. This would imply that[1] $(\kappa/r)\partial_\phi T \sim r\Lambda_0 n_e^2 T^{1/2}$, so

$$\frac{K}{r} = \frac{k_{\rm B}T}{n_e^{2/3}r} \simeq k_{\rm B}\left(\frac{2\pi\Lambda_0}{\kappa_0 L}\right)^{1/3} = \text{const.}, \qquad (11)$$

where $\kappa \simeq \kappa_0 T^{5/2}$ is the Spitzer conductivity, with $\kappa_0 \simeq 10^{-6}$ erg s^{-1}cm^{-1}K$^{-7/2}$. This is precisely the form of the universal profile (Equation (9)), and would give the correct constant provided that $L \simeq 10$ kpc.

Alternatively, consider the advection of heat in a spiral flow, either inward from the heat bath outside the core or outward from some energetic outflow originating deep within it. To find the radial velocity v, we assume the this heat flow is aligned with the spiral pattern, $\mathrm{v} = \gamma \mathrm{w}$, where the azimuthal velocity w may be found from momentum conservation in the azimuthal direction, $r^{-1}\mathrm{w}^2 \sim (\gamma r\rho)^{-1}\partial_\phi P$. These relations are rigorously derived in Section 5, in a frame rotating with the spiral pattern.

A balance between the radially advected heat and the radiative cooling would thus imply that $\Lambda_0 n_e^2 T^{1/2} \sim (3/2)\zeta n_e k_{\rm B} T v/r$, so

$$\frac{1}{L_\tau} \simeq \frac{\tau^{4/3}}{r} \simeq C\frac{(k_{\rm B}T)^{2/3}}{n_e^{2/3}r} \simeq \left(\frac{9\pi\zeta^4}{2\gamma f_{\rm g}^2}\right)^{1/3}\frac{1}{L_0^{2/3}L^{1/3}} = \text{const.}, \qquad (12)$$

where the first line restates Equation (8), and we used the estimate $\gamma \simeq 0.2$ (K12). This is precisely the form of the universal profile Equation (8) and would give the correct constant, provided that $L \simeq 1$ kpc.

The estimates (Equations (11) and (12)) are accurate only to an order of magnitude, due to the unknown geometric factors. They depend on our ad hod assumption regarding the azimuthal gradient. However, it would suffice if this assumption holds only for some part of the flow that follows the universal scaling, such as the region on one side of the CF or of the convective layer. Any such layer with $\partial_\phi \log P \propto 1/r$ flowing along the spiral pattern or with $\partial_\phi \log T \propto 1/r$ would do.

A priori, these two independent estimates of L did not have to agree. In particular, the former does not depend on G, and the latter has nothing to do with κ. Their agreement, and the plausible value of L as the base radius of the spiral and as the radius where the universal profile flattens, suggests that such conduction-supported flows may have merit. Furthermore, this supports a dynamical origin of the universal profile in Equations (8) and (9) and provides hints for a more sophisticated spiral flow modeling.

Next, we recover the universal profile from a more detailed, specific model of a spiral flow.

5. TWO-PHASE SPIRAL MODEL

Motivated by the extended spiral patterns recently observed, we generalize the core spiral flow model of K12 to the entire GA. The model focused on the two plasma phases flowing above and below the CF. Below the CF, a cold, fast flow is inferred from hydrostatic non-equilibrium measurements in many galaxy clusters (Markevitch et al. 2001; Keshet et al. 2010); this could

[1] We consider the mixed r, ϕ derivative terms in the energy (Equation (15)), as the lowest order (in r/L) azimuthal terms.

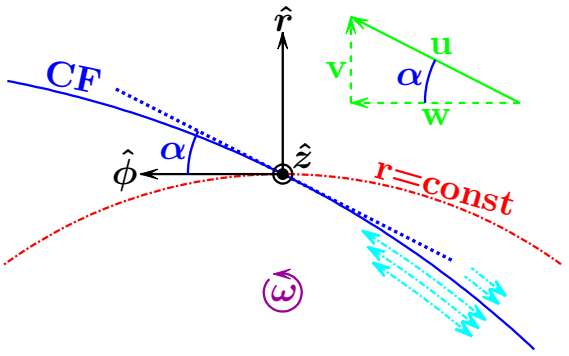

Figure 6. Illustration of the two-phase spiral flow model in the equatorial plane. The tangent (dotted line) to the CF (solid curve) forms an angle α with $\hat{\boldsymbol{\phi}}$, *i.e.,* with the circle r = constant (dot-dashed). The plasma must flow parallel to the CF. The planar velocity $\mathbf{u}$ (thick green arrow; parallel to the CF at the point analyzed) is decomposed into radial (v) and azimuthal (w) components (dashed green arrows). The flow above the CF is a slow inflow (dot-dashed cyan arrows). The flow below the CF is a fast (Keshet et al. 2010) inflow or outflow (dot-dashed cyan double headed arrows). The pattern rotates (circular arrow) about the z-axis, in the $\pm\hat{\boldsymbol{z}}$ sense for $\omega \gtrless 0$.

be either an inflow or an outflow. Above the CF, the hot phase must be a slow inflow (Keshet et al. 2010); see the illustration in Figure 6.

As the spiral has no natural scale, the model is constructed using power-law radial profiles. The interaction between the slow and fast flow components is mediated by the $\partial_\phi P \propto P$ azimuthal pressure gradient near the CF. Generalizing the model to include the gradual variation in the CF contrast q over a wide radial span, such that $\partial_\phi P \propto qP$ in the CF vicinity, yields a more realistic core structure. Surprisingly, it also reproduces the universal profile of Equations (1)–(3) throughout the GA, independent of the gravitating mass or pressure profiles. This model, focusing on the CF vicinity, is independent of the arguments made in Section 4 based on the radially declining azimuthal gradients far from the CF.

Assuming a steady state in a frame rotating at some fixed angular frequency ω, the flow is governed by the time independent continuity equation,

$$\boldsymbol{\nabla}\cdot(\rho\mathbf{U}) = 0\,, \tag{13}$$

the momentum equation,

$$\mathbf{U}\cdot\boldsymbol{\nabla}\mathbf{U} = -\rho^{-1}\boldsymbol{\nabla}P + \mathbf{g} - 2\boldsymbol{\Omega}\times\mathbf{U} - \boldsymbol{\Omega}\times(\boldsymbol{\Omega}\times\mathbf{r})\,, \tag{14}$$

and the energy equation,

$$\frac{k_{\rm B}\zeta n_e}{\Gamma-1}\left(\mathbf{U}\cdot\boldsymbol{\nabla}T + T\boldsymbol{\nabla}\cdot\mathbf{U}\right) = \boldsymbol{\nabla}\cdot(\kappa\boldsymbol{\nabla}T) - n_e^2\Lambda\left(T\right)\,. \tag{15}$$

Here, vectors such as the position vector $\mathbf{r} = \{r,\phi,z\}$ and the velocity vector $\mathbf{U} = \{\mathrm{v},\mathrm{w},U_z\}$ are written in cylindrical coordinates, $\boldsymbol{\Omega} = \omega\hat{\mathbf{z}}$ is the angular velocity vector, $\mathbf{g}$ is the gravitational acceleration (dominated by dark matter), and $\Gamma = 5/3$. For simplicity, consider simple power-law profiles for n_e and T.

5.1. *Spiral Flow Equations*

Consider first the flow confined to the equatorial plane. We use the notations of K12 (see Figure 6), but extend the analysis to the whole GA. Due to the presence of a CF, the flow (Equations (13)-(15)) in its vicinity can be cast in a simple form ((K12); continuity),

$$\lambda_\rho = -\frac{r}{\mathrm{v}}\boldsymbol{\nabla}\cdot\mathbf{U} = -\left(1+\lambda_{\rm w}+\tilde{\lambda}_z\right)\,, \tag{16}$$

momentum conservation along ϕ,

$$\frac{d}{dr}\left(\frac{\mathrm{w}^2}{2}\right) + \frac{\mathrm{w}^2}{r} = \frac{a_\phi}{\gamma} - 2\omega\mathrm{w}\,, \tag{17}$$

momentum conservation along r,

$$\frac{d}{dr}\left(\frac{\mathrm{v}^2}{2}\right) - \frac{\mathrm{w}^2}{r} = a_r + \omega^2 r + 2\omega\mathrm{w}\,, \tag{18}$$

and energy conservation,

$$\frac{\mathrm{v}\rho T}{r}\left(1+\lambda_{\rm w}+\frac{\lambda_T}{1-\Gamma}+\tilde{\lambda}_z\right) = -n_e^2\Lambda(T)\,, \tag{19}$$

where full derivatives are taken along the flow,

$$\frac{d}{dr} = \frac{\partial}{\partial r} + \frac{1}{\gamma r}\frac{\partial}{\partial\phi}\,. \tag{20}$$

Here, logarithmic derivatives $\lambda_A \equiv d\ln|A|/d\ln r$ are used (to represent an arbitrary quantity A) and $\mathbf{a} = \{a_r,a_\phi,a_z\} = -\rho^{-1}\boldsymbol{\nabla}P + \mathbf{g}$ is the inertial acceleration. Thermal conduction is neglected in this part of the flow.

These equations were derived assuming that an equatorial plane can be found, perpendicular to the z symmetry axis, in which all streamlines are approximately confined to the plane. However, they hold throughout the volume if $\mathbf{U}$ and the CF surface are perpendicular when projected onto the z-r plane; see K12. The radius of curvature perpendicular to the plane, $R_\theta = \left[1+r'(z)^2\right]^{3/2}/r''(z)$, enters the equations through the relation

$$\tilde{\lambda}_z \equiv \frac{r}{\mathrm{v}}\frac{\partial U_z}{\partial z} = \frac{r}{R_\theta}\,. \tag{21}$$

5.2. *The Fast, Cold Component*

An important clue to the nature of core spirals is the presence of fast, nearly sonic flows, found beneath well-observed CFs in the core (Keshet et al. 2010). This flow leaves the system before it significantly cools, and so it is nearly adiabatic. Equations (16) and (19) then fix its scaling (K12),

$$\lambda_\rho^f = \frac{\lambda}{\Gamma}\,;\quad \lambda_T^f = \frac{\Gamma-1}{\Gamma}\lambda\,;\quad \text{and}\quad \frac{r}{R_\theta} = -\frac{\lambda}{\Gamma}\,, \tag{22}$$

as a function of the logarithmic pressure derivative, $\lambda \equiv \lambda_P$, and

$$\lambda_{\rm w}^f = -1\,. \tag{23}$$

Here, subscripts f (s) denote the fast (slow) component.

5.3. *The Slow, Hot Component*

Although azimuthal pressure gradients are small, they must be nonzero in order to allow for a slow component (K12), and are indeed directly observed (Figure 5). To first order, one may assume (K12) that $\partial_\phi P \propto P$. However, in order to generalize the analysis to the whole GA, here we must take into account the variation in the CF contrast q with radius. We therefore assume that the

azimuthal acceleration a_ϕ of the slow component due to the pressure gradient is proportional to q,

$$2\omega \mathrm{v} \simeq a_\phi \simeq -\frac{q}{r\rho}\partial_\phi P\,. \tag{24}$$

This naturally leads to the slow velocity scaling

$$\lambda^s_{\mathrm{v}} = \lambda_q + \lambda - 1 - \lambda^s_\rho\,, \tag{25}$$

where the isobaric CF contrast follows

$$\lambda_q = \lambda^s_T - \lambda^f_T = \lambda^f_\rho - \lambda^s_\rho\,. \tag{26}$$

For the approximate $\Lambda \propto T^{1/2}$ cooling function, the energy equation (19) for the slow, cooling flow becomes

$$\lambda^s_{\mathrm{v}} + \frac{1}{2}\lambda^s_T - 1 \simeq \lambda^s_\rho\,. \tag{27}$$

Combining these with with Equation (16) gives the scaling of the slow component,

$$\lambda^s_\rho \simeq \frac{1}{7}\left[-4 + \left(3 + \frac{2}{\Gamma}\right)\lambda\right] = -\frac{4}{7} + \frac{3}{5}\lambda\,, \tag{28}$$

$$\lambda^s_T \simeq \frac{-2\lambda + 4\Gamma(1+\lambda)}{7\Gamma} = \frac{4}{7} + \frac{2}{5}\lambda\,, \tag{29}$$

$$\lambda^s_{\mathrm{v}} \simeq \frac{\Gamma + (3+\Gamma)\lambda}{7\Gamma} = \frac{1}{7} + \frac{2}{5}\lambda\,, \tag{30}$$

and

$$\lambda^s_{\mathrm{w}} \simeq \frac{-3\Gamma + (5-3\Gamma)\lambda}{7\Gamma} = -\frac{3}{7}\,, \tag{31}$$

the latter being independent of λ for $\Gamma = 5/3$.

For the entropy of the slow phase, we finally obtain

$$\lambda^s_K \simeq \frac{4\Gamma + (5-3\Gamma)\lambda}{7} = \frac{20}{21} \simeq 1\,, \tag{32}$$

flatter than found by assuming $\partial_\phi P \propto P$ in K12. As the slow component dominates the flow by mass, and strongly dominates it by volume, we approximate the overall entropy profile as $\lambda_K \simeq \lambda^s_K \simeq 1$.

The entropy power-law index in Equation (32) is very similar to the observed, universal profile in Equations (2) and (3). Over the wide radial range considered, the pressure profile cannot be approximated as a pure power law, so λ is not constant. In contrast to most other properties in the model, the entropy profile turns out to be independent of this λ (for $\Gamma = 5/3$). Hence, the entropy profile is robustly found to be a pure power law, independent of the underlying gravitating mass.

Equation (32) was derived for a $\Lambda(T) \propto T^{1/2}$ cooling function. We find that λ_K changes very little, by $[-2, +6]\%$, for more realistic cooling functions; at large radii it becomes even closer to unity.

5.4. *Properties of the generalized model*

It is interesting to examine the other properties of the generalized model. First, note that as $\rho^{-1}\partial_r P$ is fixed by the gravitational potential (to zeroth order, using hydrostatic equilibrium), and the entropy profile of the model matches the linear profile observed, the radial profiles of both the density and the temperature are guaranteed to match observations, both inside and outside of the core.

Next, consider the spiral structure. Using Equations (30) and (31), the spiral pattern is given by

$$\lambda_\gamma = \lambda^s_{\mathrm{v}} - \lambda^s_{\mathrm{w}} \simeq \frac{-2\lambda + 4\Gamma(1+\lambda)}{7\Gamma} = \frac{4}{7} + \frac{2}{5}\lambda\,, \tag{33}$$

which, using Equation (23), determines the fast radial velocity scaling,

$$\lambda^f_{\mathrm{v}} = \lambda_\gamma + \lambda^f_{\mathrm{w}} \simeq \frac{1}{7}\left[-3 + \left(4 - \frac{2}{\Gamma}\right)\lambda\right] = -\frac{3}{7} + \frac{2}{5}\lambda. \tag{34}$$

Now, using Equations (30) and (34), the radial dependence of the shear across the spiral CF is found to follow

$$\lambda^f_{\mathrm{v}} - \lambda^s_{\mathrm{v}} = \frac{-4 + (3-5\Gamma)\,\lambda}{7} = -\frac{4}{7}\,, \tag{35}$$

and the CF contrast (Equation 26) to scale as

$$\lambda_q = \frac{4 - (3-5\Gamma)\,\lambda}{7} = \frac{4}{7}\,, \tag{36}$$

more gradual than the $-4/5$ and $+4/5$ indices of K12. A summary of the scaling in the model is given in Table 3.

In addition to the more realistic thermal profiles of the generalized model, it also gives a more feasible dynamical structure. First, the radial decline in the shear and in the velocity of the fast phase, and the rise in the CF contrast are more gradual here, allowing for a more extended structure. The spiral pattern now scales as the temperature of the slow component, which dominates the flow, $\lambda_\gamma = \lambda^s_T \simeq \lambda_T$. This corresponds to a purely logarithmic spiral at the edge of the core, becoming slightly Archimedean (hyperbolic) outside (inside) the core. The perpendicular structure $\tilde{\lambda}_z$ is unchanged by our generalization, giving a prolate (closer to cylindrical) structure inside the core. At the larger radii considered here, the 3D structure becomes nearly spherical at the edge of the core, and oblate near the virial radius.

Although the contrast and shear change more slowly in the generalized model, they do vary significantly over the larger radial span considered. This may lead to large shear and contrast, in excess of observational constraints, if a spiral pattern is assumed to continuously extend all the way from the inner core ($\sim$ 10 kpc) to the GA periphery ($\sim$ 2 Mpc), as even a modest ($q = 1.1$, say) CF at 20 kpc would imply an unrealistic, $q \gtrsim 10$ beyond 1 Mpc. This would contradict the $q \sim 1.5$ contrasts observed at large radii (Rossetti et al. 2013; Urban et al. 2014; Walker et al. 2014).

An alternative is that instead of one continuous spiral, the CF is actually intermittent, composed of a series of spiral sections separated by small gaps. This possibility may be supported by the intermittent spiral patterns and CF gaps, often observed on both small (*e.g.,* Churazov et al. 2003) and large scales (Urban et al. 2014; Walker et al. 2014).

6. DISCUSSION

We study two apparently independent, universal properties of GAs: a simple power-law entropy profile extending out to the virial radius, and a ubiquitous underlying spiral pattern, apparently reaching out to the virial radius as well. We show that the former is mass-independent over a wide mass range, and argue that it

Table 3
Scaling of the two-component spiral model, for $\Gamma = 5/3$

Property A	Logarithmic derivative $\lambda_A = d\log\|A\|/d\log(r)$	
Pressure P	$\lambda \equiv \lambda_P$	
Spiral slope γ	$\frac{-2\lambda+4\Gamma(1+\lambda)}{7\Gamma} = \frac{4}{7} + \frac{2}{5}\lambda$	
Curvature	$\frac{r}{R_\theta} = -\frac{\lambda}{\Gamma}$	
	Fast phase	Slow phase
Density ρ	$\frac{\lambda}{\Gamma} = \frac{3\lambda}{5}$	$\frac{-4\Gamma+(3\Gamma+2)\lambda}{7\Gamma} = -\frac{4}{7} + \frac{3}{5}\lambda$
Temperature T	$\frac{\Gamma-1}{\Gamma}\lambda = \frac{2\lambda}{5}$	$\frac{-2\lambda+4\Gamma(1+\lambda)}{7\Gamma} = \frac{4}{7} + \frac{2}{5}\lambda$
Radial velocity v	$\frac{-3\Gamma+(4\Gamma-2)\lambda}{7\Gamma} = -\frac{3}{7} + \frac{2}{5}\lambda$	$\frac{\Gamma+(3+\Gamma)\lambda}{7\Gamma} = \frac{1}{7} + \frac{2}{5}\lambda$
Tangential velocity w	-1	$-\frac{3\Gamma-(5-3\Gamma)\lambda}{7\Gamma} = -\frac{3}{7}$
Entropy K	0	$\frac{4\Gamma+(5-3\Gamma)\lambda}{7} = \frac{20}{21}$

reflects a robust dynamical mechanism, regulating the thermal structure of the GA; models have been unable to naturally reproduce it until now. The latter reflects a long-lived, extended spiral flow, present in many, if not all, GAs. Furthermore, speculating that the two phenomena are related, we demonstrate that an extended spiral flow can naturally explain the universal thermal profile, under simple (yet somewhat ad hoc) assumptions regarding its structure. Interestingly, three independent physical arguments lead to approximately the same thermal profile, supporting these assumptions.

To quantify the thermal profile, we analyze 16 deprojected clusters and 12 deprojected groups from the literature (see Table 2), and find a good, nearly linear entropy $K(r)$ fit (see Equations (1)–(3), and Figures 1–3). The power-law index, $\lambda_K = 0.96 \pm 0.01$, is consistent with the mean $\lambda_K \sim (0.9\text{–}1.1)$ of previous studies, which used slightly different methods (see Table 1). Our tight fit is due to the wide mass range, the minimization of projection effects, and an $r > 10$ kpc selection of fit data.

A different parameterization, suggested by McCourt et al. (2012), involves the ratio τ between the cooling and free-fall times. Our data is similarly well-fit by the above $K \propto r^{\lambda_K}$, and by the relation (see Equation 7 and Figure 4) $\tau \propto r^{0.72\pm0.01}$. We are unable to determine which of these two profiles is more realistic, as they differ only by a $T^{1/3}$ factor, whereas the temperature range spanned by our data is narrow and the uncertainties are substantial. Both profiles slightly flatten for $r \lesssim 10$ kpc. This is where $\tau \sim 1$, suggesting that τ may play a more fundamental role than K in defining the thermal profile.

Previous suggestions to scale the radius by R_{500}, the entropy by $T^{0.65}$, or both, only diminish the correlation; the R_{500} scaling effectively splits the GAs by mass. We find no difference between GAs with versus those without Hα filaments, nor any $\tau(r)$ profiles showing a minimum; this differs from previous reports, but is consistent with the absence of an 'entropy floor' (*e.g.,* Panagoulia et al. 2014).

We find that the giant elliptical galaxy M49, which resides in the outskirts of the Virgo cluster and harbors an AGN, approximately follows the same universal thermal profile (see Figures 1 and 4). It would be interesting to see if the universal profile characterizes all AGN harboring systems, and thus more generally applies not only for GAs.

The universal thermal profile may seem surprising, as it appears to be oblivious to the temperature peak at the edge of the core and to the virial shock at the edge of the GA, and is robust to the presence of the ongoing cooling, merger, and AGN activity. Furthermore, the profile (in either of the two idealized forms we derive, Equations (8) or (9)) is not naturally obtained from the flow equations without introducing some large number or a dimensional constant, even if conduction and cooling are taken into account. This suggests some non-local mechanism.

The entropy profile is usually attributed to the self-similar evolution of primordial gas crossing the virial shock. However, we find that this model, without baryonic effects, does not provide a good description to the data, for the following reasons: *(i)* the observed profile shows no break as one crosses into the core, where radiative cooling becomes significant and the self-similarity is expected to break; *(ii)* the self-similar model predicts a $K_{100} \propto M^{0.26}$ correlation between the entropy and the GA mass, which is inconsistent with our results (see Figure 3) by more than 8σ; *(iii)* the normalization of the entropy in the self-similar model is inconsistent with our results (at significance levels ranging between 1σ and 20σ for different clusters, and $> 6.5\sigma$ on average; see Figure 3); *(iv)* The self-similar model predicts a radial power law $\lambda_K \approx 1.2$ (V05), which is inconsistent with our results at $> 8\sigma$ for the full $r > 10$ kpc sample, or $> 4\sigma$ when limited to radii outside the core ($0.3 < r/R_{500} < 1.5$; see Figure 1).

Alternative mechanisms, such as non-standard heat conduction or turbulent heating, require fine tuning. We therefore argue that a robust, dynamical, non-local mechanism is needed to sustain the universal profile.

A natural candidate for such a dynamical mechanism involves the spiral flow, as it too is ubiquitous, spans the same radial range, and similarly overlaps the CC where radiative cooling plays an important role. This suggests that the universal profile and the spiral flow can both be regarded as manifestations of the cooling problem. To examine if a spiral flow can regulate the structure of the GA and enforce the universal thermal profile, some assumption must be made regarding the azimuthal gra-

dients, in particular those of pressure (*e.g.,* Figure 5) or temperature.

The simplest assumption involving a new length scale, motivated by the slight Archimedean nature of CC spirals (K12) and by the necessary presence of a convective layer (Appendix B), is that in some part of the flow, azimuthal gradients diminish with r as $\partial_\phi \log A \sim L/(2\pi r)$, where L is an a priori unknown length scale. A balance between cooling and azimuthal heat conduction thus recovers the $K(r) \propto r$ profile (see Equations (9) and (11)), while independently requiring a balance between cooling and radial heat advection reproduces the $\tau \propto r^{3/4}$ relation (see Equations (8) and (12)). Interestingly, although these two arguments are of a very different physical nature, both give similar $L \sim$ 1–10 kpc scales. Moreover, this range of L turns out to be quite natural, signaling the regime where τ approaches unity and the thermal profile flattens, so no artificial scale is introduced. Indeed, this is also the typical radius at the base of the spiral, where radial and azimuthal gradients are expected to become comparable.

These conclusions confirm the dynamical origin of the universal profile, support the ad hoc azimuthal gradient assumption, and provide hints for more sophisticated spiral flow modeling. The universal thermal profile, in particular its normalization, shows no correlation with GA mass, as demonstrated in Figures. 2 and 3. This strongly constrains the mechanism behind the thermal profile. In the simple spiral flow modeling of section 4, this corresponds to the length scale L being a universal, mass-independent constant.

A third independent way to see how a spiral flow could regulate the universal profile is to analyze the flow along the CFs. To do so we generalize the core spiral flow model of K12 to the entire GA. Here, the flow is approximated as a combination of fast and slow components, interacting through the azimuthal pressure gradients in the CF vicinity. To extend the model over a large radial span, we incorporate the CF contrast q to obtain $\partial_\phi P \sim qP$. This expression yields more realistic thermal profiles within the core, and a more feasible dynamical structure than found in K12. Surprisingly, it also reproduces an approximately linear $K(r)$ profile throughout the GA (see Equation 32), consistent with observations, and independent of the (non-power-law) radial pressure profile. Consequently, all the observed thermal profiles are reproduced, regardless of the underlying mass distribution, both in and beyond the core, out to the virial radius.

A spiral flow may alleviate the cooling problem (K12), because it can (i) advect heat inward from the periphery or outward from the AGN; (ii) distribute energy evenly in space and time; (iii) provide a feedback loop by regulating the flow rate; and (iv) operate with little to no mass accretion. We strengthen this model by showing how a careful balance between cooling, radial heat advection, and azimuthal heat conduction consistently yields the universal profile under plausible assumptions.

The generalized two-component spiral model provides additional information regarding the thermal and dynamical structure of GAs (see Table 3). Most importantly, such models yield a mild temperature drop toward the GA center, avoiding the cooling problem (K12). With increasing r, the CF manifold is predicted to gradually transition from mildly prolate to oblate, and from a slightly hyperbolic to a mildly Archimedean spiral. The CFs in the model show an increasing $q \propto r^{4/7}$ contrast, and a decreasing $\sim r^{-4/7}$ shear. Although this allows for more extended CFs than in K12, such CFs cannot continuously extend from the GA center out to its outskirts, suggesting some pattern intermittency, in accord with observations (*e.g.,* Churazov et al. 2003; Urban et al. 2014; Walker et al. 2014).

A central open question is the mechanism driving the spiral flow and depositing the necessary angular momentum; see discussion in K12. Our results do not distinguish between the two previous suggestions for the mechanism driving the spiral - either mergers or strong AGN activity. Our assumptions regarding the azimuthal gradients are somewhat ad hoc, as one could have conjectured more complicated azimuthal profiles such as $\partial_\phi P \propto (L/r)^\beta P$ with some $\beta \neq 1$, or $\partial_\phi P \propto (q-1)P$. In general, however, these would have led to non-power-law scalings, or to inconsistencies. A more sophisticated and in part numerical modeling of spiral flows is needed in order to quantify these gradients and resolve the 3D structure of the flow.

Spiral flows stabilized by shear-amplified magnetic fields, featuring a fast flow under the CF, are already found in magnetohydrodynamic (MHD) simulations of single clusters undergoing a merger (ZuHone et al. 2011). Spiral flows were also produced in simulations incorporating radiative cooling (severely limiting their lifetime; ZuHone et al. 2010) and different forms of viscosity (Roediger et al. 2013) and heat conduction (ZuHone et al. 2013). To produce a physically viable model for large-scale spiral flows, simulations would need to combine the above elements in a self-consistent fashion. Such simulations would need to resolve the spiral structure both at its base ($\lesssim$ 1 kpc) scale, and its outer (virial) scale. The observational evidence outlined above suggests that additional physical processes, notably the virial shock and AGN feedback, *e.g.,* in the form of radio bubbles, are important ingredients of the spiral flow and should be incorporated into simulations. A successful simulation should show a long-lived core, and reproduce the observed radial scalings, in particular the universal profile and the structure of the 3D CF surface gradually uncovered by observations.

Such simulations, as well as future observations, will directly test our results. In particular, they could either refine or rule out our spiral flow suggestion for the dynamical mechanism regulating the universal profile. For example, the presence of a fast flow below the CF, which is based on present observations and simulations, is a key assumption of the spiral flow model; it will be critically tested with far greater accuracy by future observations and simulations. A realistic spiral flow simulation, incorporating the physical processes outlined above, would directly test our approximation of two-phases composing the spiral, and gauge the simplified power-law scalings we derive. Simulations and observations would also test additional predictions of the model, such as the presence of a convective zone, a CF intermittency, and entrained radio bubbles (Keshet 2012). The role of the spiral flow in regulating the universal profile will be ruled out if

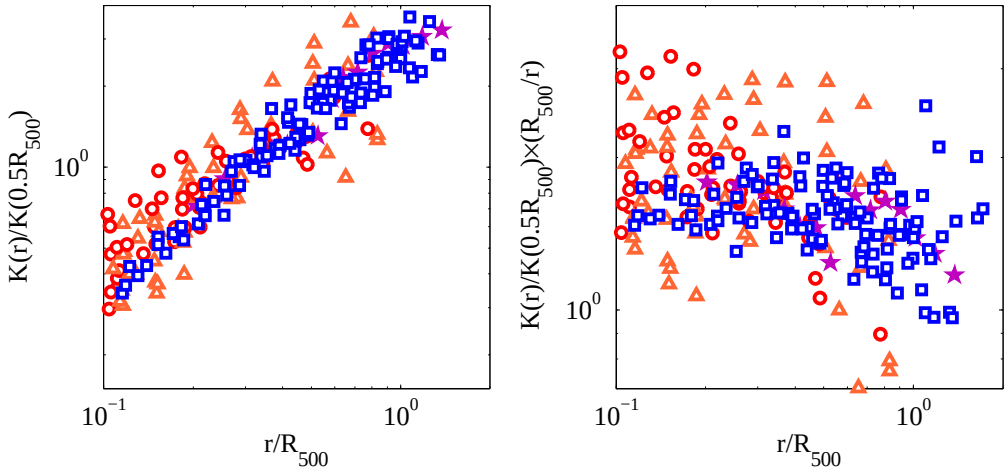

Figure 7. Left: the entropy (scaled to the entropy at $0.5R_{500}$) as a function of the scaled radius. Right: radially normalized entropy, $K(r)/r$ (scaled to $0.5R_{500}$), plotted to enhance any deviation from a power-law behavior. The symbols are the same as in Figure 1.

this profile is observed in the clear absence of any underlying spiral pattern, or if simulations conclusively show that spiral flows are non-universal, *e.g.,* greatly depending upon initial conditions.

Future deprojected profiles of GAs, in particular at the low and high temperature ends, should distinguish between the two forms of the universal profile (Equations 2 versus 7). Deep observations of GAs can place strong constraints on the spiral pattern, on the structure of the CF surface, and on the flow itself through, for example, line-of-sight velocity measurements. These constraints would allow for a better modeling of the underlying spiral flow, and would directly test the azimuthal gradients postulated above, as well as the flow and CF properties they imply. Our results suggest that the diffuse gas survives down to scales where $\tau \sim 1$, smaller than thought so far, where the strong competition between gravity and cooling is likely to have interesting consequences.

The identification of spiral structures in galaxy clusters is challenging even at small radii, due to its subtlety and to resolution and projection effects. Identifying spiral structures at large radii is even more difficult, due to the lower $F_{\rm X}$. Therefore, the recently identified large-scale spiral structures in three clusters – Perseus (Simionescu et al. 2012), A2142 (Rossetti et al. 2013), and RXJ2014 (Walker et al. 2014) – and observational hints of such structures in several more deep observations (*e.g.,* A496, A3558, A85, A2052, and A2199; see Rossetti 2014) suggest that this phenomenon is ubiquitous. In our spiral model for the universal profile, spiral structures are inevitable at large radii. Deeper observations will test this prediction.

This research has received funding from the European Union Seventh Framework Programme (FP7/2007-2013) under grant agreement n$^{\rm o}$ 293975, from an IAEC-UPBC joint research foundation grant, and from an ISF-UGC grant.

APPENDIX

A. TESTING A POSSIBLE ENTROPY FLATTENING AT THE OUTSKIRTS

To further test any possible flattening of the entropy in the outskirts of clusters (*e.g.,* the *Suzaku* analysis in Walker et al. 2012), Figure 7 shows the entropy in our sample using the method of Walker et al. (2012); namely, scaling the entropy to its value at $0.5R_{500}$ and to a linear radial profile, and scaling the radius to R_{500}. Unlike Walker et al. (2012), we see no significant flattening in the entropy at cluster outskirts, in accordance with stacked *ROSAT* (Eckert et al. 2012) and *Chandra* (Morandi et al. 2015) observations. This has been discussed, based on the data used here, in Eckert et al. (2012).

B. GENERALIZED SCHWARZSCHILD CRITERION

We extend the Schwarzschild criterion (Schwarzschild 1958; Lebovitz 1965) for convective stability, $\partial_r K > 0$, to an anisotropic medium harboring a spiral flow, implying that a mixing layer must form in a realistic spiral flow. Such flows show CFs with an entropy contrast $q_K = K_o/K_i$, where subscript i (o) represents the region just inside (outside) the CF. Therefore, the azimuthal entropy derivative must at least somewhere satisfy $\partial_\phi K_i \geq (q_K - 1)K_i/2\pi$. At that point, convective stability against perturbations along both r and ϕ would require

$$\lambda_K \simeq \lambda_{K_i} = \frac{r}{K_i}\left(\frac{\partial K_i}{\partial r} + \frac{1}{\gamma r}\frac{\partial K_i}{\partial \phi}\right) > \frac{1+\gamma}{\gamma K_i}\frac{\partial K_i}{\partial \phi} \geq \frac{(q_K - 1)(1+\gamma)}{2\pi\gamma}\,, \tag{B1}$$

where the first approximate equality assumes a self-similar spiral structure, so λ_K can be measured just inside the CF, and in the first inequality we require that azimuthal perturbations do not lead to larger radial displacements; the (weaker) Schwarzschild criterion would merely remove the γ term in the numerators. The entropy profile approximately follows $\lambda_K \simeq 1$, the spiral pattern roughly shows $\gamma \simeq 0.2$ (K12), and the temperature contrast q yields $q_K \simeq q^{5/3} \simeq 3$.

Hence, Equation (B1) breaks down somewhere, and a convective layer is expected to form.

Equation (B1) indicates that the azimuthal derivative of the entropy cannot be constant, as the entire medium will then be convectively unstable. Hence, the derivative must diminish across a large sector, as assumed in Section 4.

REFERENCES

Ascasibar, Y., & Markevitch, M. 2006, ApJ, 650, 102, astro-ph/0603246
Birzan, L., Rafferty, D. A., McNamara, B. R., Wise, M. W., & Nulsen, P. E. J. 2004, ApJ, 607, 800, astro-ph/0402348
Blanton, E. L., Randall, S. W., Clarke, T. E., Sarazin, C. L., McNamara, B. R., Douglass, E. M., & McDonald, M. 2011, ApJ, 737, 99, 1105.4572
Bulbul, G. E., Smith, R. K., Foster, A., Cottam, J., Loewenstein, M., Mushotzky, R., & Shafer, R. 2012, ApJ, 747, 32, 1110.4422
Canning, R. E. A. et al. 2013, MNRAS, 435, 1108, 1305.0050
Cavagnolo, K. W., Donahue, M., Voit, G. M., & Sun, M. 2009, ApJS, 182, 12, 0902.1802
Cavaliere, A., & Lapi, A. 2013, Phys. Rep., 533, 69, 1308.6673
Churazov, E., Forman, W., Jones, C., & Böhringer, H. 2003, ApJ, 590, 225, arXiv:astro-ph/0301482
Churazov, E., Sunyaev, R., Forman, W., & Böhringer, H. 2002, MNRAS, 332, 729, astro-ph/0201125
Clarke, T. E., Blanton, E. L., & Sarazin, C. L. 2004, ApJ, 616, 178, arXiv:astro-ph/0408068
Dolag, K., Jubelgas, M., Springel, V., Borgani, S., & Rasia, E. 2004, ApJL, 606, L97, astro-ph/0401470
Donahue, M., Horner, D. J., Cavagnolo, K. W., & Voit, G. M. 2006, ApJ, 643, 730, astro-ph/0511401
Dunn, R. J. H., & Fabian, A. C. 2006, MNRAS, 373, 959, astro-ph/0609537
Eckert, D., Ettori, S., Molendi, S., Vazza, F., & Paltani, S. 2013a, A&A, 551, A23, 1301.0624
Eckert, D., Molendi, S., Vazza, F., Ettori, S., & Paltani, S. 2013b, A&A, 551, A22, 1301.0617
Eckert, D., Roncarelli, M., Ettori, S., Molendi, S., Vazza, F., Gastaldello, F., & Rossetti, M. 2013c, ArXiv e-prints, 1310.8389
Eckert, D. et al. 2012, A&A, 541, A57, 1111.0020
Eckmiller, H. J., Hudson, D. S., & Reiprich, T. H. 2011, A&A, 535, A105, 1109.6498
Fabian, A. C. 2012, ARA&A, 50, 455, 1204.4114
Finoguenov, A., Davis, D. S., Zimer, M., & Mulchaey, J. S. 2006, ApJ, 646, 143, astro-ph/0611858
Gastaldello, F., Buote, D. A., Brighenti, F., Mathews, W. G., Temi, P., & Ettori, S. 2009a, in American Institute of Physics Conference Series, Vol. 1201, American Institute of Physics Conference Series, ed. S. Heinz & E. Wilcots, 237–240, 0909.0600
Gastaldello, F., Buote, D. A., Temi, P., Brighenti, F., Mathews, W. G., & Ettori, S. 2009b, ApJ, 693, 43, 0807.3526
Gastaldello, F. et al. 2013, ApJ, 770, 56, 1304.5478
Ghizzardi, S., De Grandi, S., & Molendi, S. 2014, A&A, 570, A117, 1407.6814
Ghizzardi, S., Rossetti, M., & Molendi, S. 2010, A&A, 516, A32, 1003.1051
Giacintucci, S., Markevitch, M., Brunetti, G., ZuHone, J. A., Venturi, T., Mazzotta, P., & Bourdin, H. 2014, ApJ, 795, 73, 1403.2820
Gitti, M., O'Sullivan, E., Giacintucci, S., David, L. P., Vrtilek, J., Raychaudhury, S., & Nulsen, P. E. J. 2010, ApJ, 714, 758, 0912.3013
Gonzalez, A. H., Sivanandam, S., Zabludoff, A. I., & Zaritsky, D. 2013, ApJ, 778, 14, 1309.3565
Green, D. A. 2011, Bulletin of the Astronomical Society of India, 39, 289, 1108.5083
Humphrey, P. J., Buote, D. A., Brighenti, F., Flohic, H. M. L. G., Gastaldello, F., & Mathews, W. G. 2012, ApJ, 748, 11, 1106.3322
Jetha, N. N., Hardcastle, M. J., Babul, A., O'Sullivan, E., Ponman, T. J., Raychaudhury, S., & Vrtilek, J. 2008, MNRAS, 384, 1344, 0712.1150
Johnson, R., Ponman, T. J., & Finoguenov, A. 2009, MNRAS, 395, 1287, 0902.2781
Johnson, R. E., Markevitch, M., Wegner, G. A., Jones, C., & Forman, W. R. 2010, ApJ, 710, 1776, 1001.2441
Kaastra, J. S. et al. 2004, A&A, 413, 415, astro-ph/0309763
Keshet, U. 2012, ApJ, 753, 120, 1111.2337
Keshet, U., Markevitch, M., Birnboim, Y., & Loeb, A. 2010, ApJL, 719, L74, 0912.3526
Khosroshahi, H. G., Jones, L. R., & Ponman, T. J. 2004, MNRAS, 349, 1240, astro-ph/0401023
Kraft, R. P. et al. 2011, ApJ, 727, 41
Kravtsov, A. V., & Borgani, S. 2012, ARA&A, 50, 353, 1205.5556
Laganá, T. F., Andrade-Santos, F., & Lima Neto, G. B. 2010, A&A, 511, A15, 0911.3785
Lebovitz, N. R. 1965, ApJ, 142, 229
Lewis, A. D., Buote, D. A., & Stocke, J. T. 2003, ApJ, 586, 135, arXiv:astro-ph/0209205
Machacek, M. E., Jerius, D., Kraft, R., Forman, W. R., Jones, C., Randall, S., Giacintucci, S., & Sun, M. 2011, ApJ, 743, 15, 1108.5229
Mahdavi, A., Finoguenov, A., Böhringer, H., Geller, M. J., & Henry, J. P. 2005, ApJ, 622, 187, astro-ph/0502362
Markevitch, M., & Vikhlinin, A. 2007, Phys. Rep., 443, 1, astro-ph/0701821
Markevitch, M., Vikhlinin, A., & Forman, W. R. 2003, in Astronomical Society of the Pacific Conference Series, Vol. 301, Matter and Energy in Clusters of Galaxies, ed. S. Bowyer & C.-Y. Hwang, 37, astro-ph/0208208
Markevitch, M., Vikhlinin, A., & Mazzotta, P. 2001, ApJL, 562, L153, astro-ph/0108520
Mazzotta, P., Markevitch, M., Vikhlinin, A., Forman, W. R., David, L. P., & van Speybroeck, L. 2001, ApJ, 555, 205, astro-ph/0102291
McCourt, M., Sharma, P., Quataert, E., & Parrish, I. J. 2012, MNRAS, 419, 3319, 1105.2563
McNamara, B. R., & Nulsen, P. E. J. 2007, ARA&A, 45, 117, 0709.2152
Morandi, A., Sun, M., Forman, W., & Jones, C. 2015, MNRAS, 450, 2261, 1501.04095
Nulsen, P. E. J. et al. 2013, ApJ, 775, 117, 1307.8072
Osmond, J. P. F., & Ponman, T. J. 2004, MNRAS, 350, 1511, astro-ph/0402439
O'Sullivan, E., Giacintucci, S., David, L. P., Vrtilek, J. M., & Raychaudhury, S. 2010, MNRAS, 407, 321, 1004.5501
O'Sullivan, E., Worrall, D. M., Birkinshaw, M., Trinchieri, G., Wolter, A., Zezas, A., & Giacintucci, S. 2011, MNRAS, 416, 2916, 1106.2449
Panagoulia, E. K., Fabian, A. C., & Sanders, J. S. 2014, MNRAS, 438, 2341, 1312.0798
Peterson, J. R., & Fabian, A. C. 2006, Phys. Rep., 427, 1, astro-ph/0512549
Piffaretti, R., Jetzer, P., Kaastra, J. S., & Tamura, T. 2005, A&A, 433, 101, astro-ph/0412233
Planck Collaboration et al. 2013, A&A, 550, A131, 1207.4061
Ponman, T. J., Sanderson, A. J. R., & Finoguenov, A. 2003, MNRAS, 343, 331, astro-ph/0304048
Pratt, G. W., & Arnaud, M. 2005, A&A, 429, 791, astro-ph/0406366
Pratt, G. W. et al. 2010, A&A, 511, A85, 0909.3776

Pratt, G. W., Arnaud, M., & Pointecouteau, E. 2006, A&A, 446, 429, astro-ph/0508234
Quataert, E. 2008, ApJ, 673, 758, 0710.5521
Rafferty, D. A., McNamara, B. R., & Nulsen, P. E. J. 2008, ApJ, 687, 899, 0802.1864
Randall, S. W., Clarke, T. E., Nulsen, P. E. J., Owers, M. S., Sarazin, C. L., Forman, W. R., & Murray, S. S. 2010, ApJ, 722, 825, 1008.2921
Randall, S. W. et al. 2011, ApJ, 726, 86, 1006.4379
Randall, S. W., Jones, C., Markevitch, M., Blanton, E. L., Nulsen, P. E. J., & Forman, W. R. 2009, ApJ, 700, 1404, 0904.0610
Reiprich, T. H., & Böhringer, H. 2002, ApJ, 567, 716, arXiv:astro-ph/0111285
Reiss, I., & Keshet, U. 2014, Physical Review Letters, 113, 071302
Roediger, E., Brüggen, M., Simionescu, A., Böhringer, H., Churazov, E., & Forman, W. R. 2011, MNRAS, 413, 2057, 1007.4209
Roediger, E., Kraft, R. P., Forman, W. R., Nulsen, P. E. J., & Churazov, E. 2013, ApJ, 764, 60, 1211.4874
Rossetti, M. 2014, in The X-ray Universe 2014, 312
Rossetti, M., Eckert, D., De Grandi, S., Gastaldello, F., Ghizzardi, S., Roediger, E., & Molendi, S. 2013, A&A, 556, A44, 1305.2420
Russell, P. A., Ponman, T. J., & Sanderson, A. J. R. 2007, MNRAS, 378, 1217, astro-ph/0703010
Rybicki, G. B., & Lightman, A. P. 1986, Radiative Processes in Astrophysics (Wiley)
Sanders, J. S., Fabian, A. C., Frank, K. A., Peterson, J. R., & Russell, H. R. 2010, MNRAS, 402, 127, 0910.3793
Sanders, J. S., Fabian, A. C., Hlavacek-Larrondo, J., Russell, H. R., Taylor, G. B., Hofmann, F., Tremblay, G., & Walker, S. A. 2014, MNRAS, 444, 1497, 1407.8008
Sanders, J. S., Fabian, A. C., & Taylor, G. B. 2009, MNRAS, 396, 1449, 0904.1374
Sanderson, A. J. R., O'Sullivan, E., & Ponman, T. J. 2009, MNRAS, 395, 764, 0902.1747
Schwarzschild, M. 1958, Structure and evolution of the stars. (Princeton University Press)
Sharma, P., McCourt, M., Quataert, E., & Parrish, I. J. 2012, MNRAS, 420, 3174, 1106.4816
Simionescu, A. et al. 2012, ApJ, 757, 182, 1208.2990
Soker, N. 2010, ArXiv e-prints, 1007.2249
Tanaka, T., Kunieda, H., Hudaverdi, M., Furuzawa, A., & Tawara, Y. 2006, PASJ, 58, 703
Tozzi, P., & Norman, C. 2001, ApJ, 546, 63, arXiv:astro-ph/0003289
Urban, O. et al. 2014, MNRAS, 437, 3939, 1307.3592
Urban, O., Werner, N., Simionescu, A., Allen, S. W., & Böhringer, H. 2011, MNRAS, 414, 2101, 1102.2430
Venturi, T., Rossetti, M., Bardelli, S., Giacintucci, S., Dallacasa, D., Cornacchia, M., & Kantharia, N. G. 2013, A&A, 558, A146, 1308.0992
Vikhlinin, A. A., Kravtsov, A. V., Markevich, M. L., Sunyaev, R. A., & Churazov, E. M. 2014, Physics Uspekhi, 57, 317
Voit, G. M., Kay, S. T., & Bryan, G. L. 2005, MNRAS, 364, 909, astro-ph/0511252
Walker, S. A., Fabian, A. C., & Sanders, J. S. 2014, MNRAS, 441, L31, 1402.6894
Walker, S. A., Fabian, A. C., Sanders, J. S., & George, M. R. 2012, MNRAS, 427, L45, 1208.5950
Werner, N., Zhuravleva, I., Churazov, E., Simionescu, A., Allen, S. W., Forman, W., Jones, C., & Kaastra, J. S. 2009, MNRAS, 398, 23, 0904.0254
Zakamska, N. L., & Narayan, R. 2003, ApJ, 582, 162, astro-ph/0207127
Zhuravleva, I. et al. 2014, Nature, 515, 85, 1410.6485
ZuHone, J. A., Markevitch, M., & Johnson, R. E. 2010, ApJ, 717, 908, 0912.0237
ZuHone, J. A., Markevitch, M., & Lee, D. 2011, ApJ, 743, 16, 1108.4427
ZuHone, J. A., Markevitch, M., Ruszkowski, M., & Lee, D. 2013, ApJ, 762, 69, 1204.6005